Acoustic Analysis of Counter Rotating Open Rotors with a Locked Blade Row

D. A. Smith * and A. Filippone.†
Aviation and the Environment, University of Manchester, M13 9PL, UK.

G. N. Barakos‡
CFD Laboratory, University of Glasgow, G12 8QQ, UK.

Counter Rotating Open Rotors (CROR) have the potential to reduce environmental emissions thanks to their high propulsive efficiency. However, there are a number of concerns surrounding their acoustic emissions. This contribution presents a novel multi-configuration CROR that offers considerable noise reductions. In particular, we consider locking either fore or aft rotor during take-off, with the running rotor providing the required thrust. During cruise, both rotors are operated to retain the high efficiency of the CROR. A coupled Computational Fluid Dynamics-Computational Aeroacoustics analysis (CFD-CAA) has shown the potential of this multi-configuration concept to offer substantial noise reductions when compared to a baseline CROR. During a simulated constant-altitude flyover at take-off conditions, reductions of 3.5 dBA and 7.9 dBA have been demonstrated when either fore or aft row is locked, respectively. Using the EPNL metric, this result corresponded to7 EPNLdB and 12 EPNLdB, respectively, for the same flyover.

Nomenclature

$BEMT$	=	Blade Element Momentum Theory
CAA	=	Computational AeroAcoustics
CFD	=	Computational Fluid Dynamics
$CROR$	=	Counter Rotating Open Rotor
$EPNL$	=	Effective Perceived Noise Level
$HFWH$	=	Helicopter Ffowcs Williams-Hawkings — Acoustic code
HMB	=	Helicopter Multi-Block — CFD solver
$OASPL$	=	OverAll Sound Pressure Level
SPL	=	Sound Pressure Level

*PhD Student, Department of MACE, The University of Manchester, M13 9PL, UK
†Reader, Department of MACE, The University of Manchester, M13 9PL, UK, Senior AIAA Member.
‡Professor, School of Engineering, University of Glasgow, G12 8QQ, UK

$uRANS$	=	unsteady Reynolds Averaged Navier-Stokes
c	=	Blade element chord
c_0	=	Speed of sound
C_{l_d}	=	Design lift coefficient
D	=	Rotor diameter = $2R$
E	=	Total energy
$\boldsymbol{F}_i/\boldsymbol{F}_v$	=	Vector of inviscid/viscous fluxes
g	=	Axial distance between rotors
M	=	Mach number
M_n	=	Mach number in normal direction
M_r	=	Mach number in radiation direction
M_T	=	Tip Mach number
$\boldsymbol{n}$	=	Unit normal
N	=	Blade count
p'	=	Acoustic pressure
p_s	=	Blade surface pressure
Q	=	Torque
r_h	=	Hub radius
R	=	Tip radius
$\boldsymbol{R}$	=	Vector of flux residuals
$\mathcal{R}$	=	Source-observer distance
$\boldsymbol{S}$	=	Source term accounting for rotor rotation
S	=	Blade surface
t	=	Time
t/c	=	Thickness-chord ratio
T	=	Thrust
u, v, w	=	Cartesian velocity components
$\mathcal{V}$	=	Control Volume
$\mathcal{V}$	=	Cell volume
V_∞	=	Free stream velocity
$\boldsymbol{W}$	=	Vector of conserved variables
$\boldsymbol{x}$	=	Observer location

β = Blade setting angle

η = Propulsive efficiency, $V_\infty T/\Omega Q$

θ = Polar flyover angle

Θ = Angle between normal and radiation direction

ρ = Fluid density

σ = Blade solidity, $Nc/\pi R$

ψ = Azimuth angle

Ω = Rotational speed

$[\cdot]_{1,2}$ = Fore/aft rotor

I. Introduction

The aviation industry is facing increasing pressure to reduce emissions. As a result of this pressure, there is a renewed interest in the Counter Rotating Open Rotor (CROR) concept. The CROR can offer significant improvements in efficiency due to the counter-rotation of the aft rotor removing residual swirl from the fore row. Furthermore, without the drag of a duct and their high bypass ratios, CROR can significantly reduce aircraft emissions when compared to conventional aircraft propulsion systems [1].

General Aviation contributes highly to global aviation emissions. However, it does not receive the same attention as commercial aviation. Thus, we have focussed on the application of CROR to general aviation aircraft. The use of CROR on general aviation aircraft affords several benefits, including increased control in the event of an engine failure and increased fuel efficiency. The use of CROR also allows for easy integration of hybrid engine architectures.

Despite their increased fuel efficiency, without a duct to limit noise propagation, there are concerns surrounding the noise levels of CROR. Being highly tonal, with significant noise levels in all directions across a wide frequency range, CROR noise presents a complex problem. Nonetheless, a number of concepts have been explored to reduce CROR noise.

Weckmüller & Guérin [2] investigated the use of serrated trailing edges to reduce wake interaction noise. This concept aims at increasing the mixing of the fore wake and decrease the wake deficit and resulting interaction with the aft rotor. From the numerical analysis, Weckmüller & Guérin found that the serrations offered an 0.2dB reduction in OASPL. This lower than expected reduction was attributed to the dominance of the tip vortex interaction clouding any reduction due to serrations. Jaron et al. [3] revisited the concept using an evolutionary algorithm to optimise the serration design. Jaron et al. identified a maximum noise reduction of 1 dB from the optimisation of the serrations.

Delattre & Falissard [4] and Delattre et al. [5] numerically investigated the use of a small protuberance on the leading-edge of the fore rotor to reduce the wake interaction noise. The small protuberance, placed at 80% of the span,

was found to reduce the dominant interaction tones when compared to the unmodified CROR. Furthermore, the authors found it had only a small impact on the aerodynamic performance. The role of the protuberance was to prevent the mixing of the leading-edge and tip vortices, resulting in an overall weaker interaction. Khalid et al. [6] also studied the control of the leading-edge vortex. In this work, the authors discussed the use of additional camber and modified thickness to prevent the roll-up of the leading-edge vortex.

Trailing edge blowing has also been proposed to control the wake deficit. A number of authors have performed numerical investigations into the use of trailing edge blowing on the fore rotor to reduce wake interaction noise, see. Refs. [7–11]. The concept was found to make a significant impact in reducing the wake deficit and its resulting interaction with the aft row. Furthermore, the use of trailing edge blowing was found to reduce noise levels across most polar directivities. Noise reductions were more pronounced for the interactions tones, having only a small impact on the self tones.

Zachariadis et al. [12] proposed changes to the rotor rotational speed and setting angles at take-off to reduce the noise of a highly loaded CROR. These changes resulted in a reduction of the fore wake contraction and hence weaker downstream interactions. However, whilst this reduced the interaction component, an increase in self-noise was observed. Delatre & Fallisard [13] also investigated the loading of the fore rotor by studying the effect of torque ratio on CROR noise. When the aft torque was greater than the fore, the reduced loading of the fore rotor resulted in a reduction in the interaction noise due to the weaker wake.

In this contribution, we present a novel CROR embodiment to significantly reduce CROR noise. In particular, we focus on the application to general aviation aircraft (light propeller-driven aircraft with a maximum take-off mass $< 8,618$ kg). Our concept considers variable configuration blade rows. We propose locking either fore or aft blade row during take-off, climb-out and approach conditions. During cruise, both rotors are operated at their design speed to utilise the high efficiency of the CROR configuration. This configuration only requires that a single rotor can deliver the take-off thrust. Whilst this will increase the self-noise of the running rotor, this should be counteracted by a reduction in the interaction noise which dominates the low-speed operating points.

The proposed embodiments are investigated using a coupled CFD-CAA computational strategy that allows for detailed flowfield and noise component comparisons. This work will proceed with a description of the test cases and the computational strategy used for the analysis. Following this, a detailed aerodynamic analysis is carried out before the noise emissions are reviewed.

II. Description of Test Cases

In the analysis we consider three embodiments (Figure 1): (i) both rotors running (baseline); (ii) fore rotor locked, with aft rotor running (fore-locked); (iii) aft rotor locked, with fore rotor running (aft-locked). For cases with a locked blade row, the operative rotor is trimmed to deliver the total thrust (i.e. the required thrust plus the drag due to locked

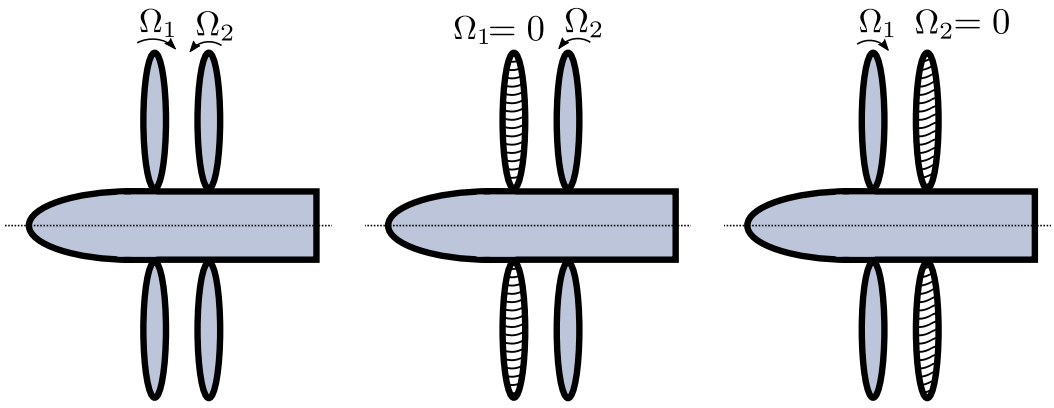

(a) *Baseline CROR* (b) *Fore-locked CROR* (c) *Aft-locked CROR*

Fig. 1 *Baseline and inoperative configurations.*

blade row), whilst the locked row is trimmed to minimise torque. For the case with both rotors running, the thrust is split equally between both rotors. Although an equal thrust split is not necessarily required in practice, it allows for greater identification of the noise sources from each rotor. In particular, if the rotors are equally loaded, the self-noise will be comparable, and the resulting differences in noise will result from the interaction sources. The analysis is performed at take-off conditions ($M = 0.2$). We consider the isolated CROR in axial flight and compare both polar and azimuthal directivities. In line with general aviation certification, the A-weighted SPL is used to compare noise levels between each configuration [14].

A tractor CROR has been designed to be representative of a general aviation propulsion system. Using the FLIGHT aircraft performance code [15, 16] to simulate the Beechcraft 350i at take-off conditions, the CROR configuration has been sized to deliver a take-off thrust of 6 kN. With a reference tip speed of $M_T = 0.46$ and fore and aft blade count equal to 4 ($N_1 = N_2 = 4$), a 3 m diameter CROR resulted. Note that both rotors were of equal diameter, i.e. no tip clipping was used. Although clipping of the aft rotor is typically used on modern CROR, it is not used here so that the differences between the locked-row configurations can be compared more fairly. Table 1 presents the notable design features of the CROR configuration. The spanwise geometry was described by the SR2 design [17], shown in Figure 2.

Table 1 *Rotor design parameters.*

Parameter	σ	$R_1 = R_2$ [m]	r_h/R	g/R	M_T
Value	0.36	1.5	0.24	0.4	0.46

For each configuration, the required setting angles were computed using a Blade Element Momentum Theory (BEMT) method extended for CROR [18]. Table 2 presents the computed setting angles for each configuration.

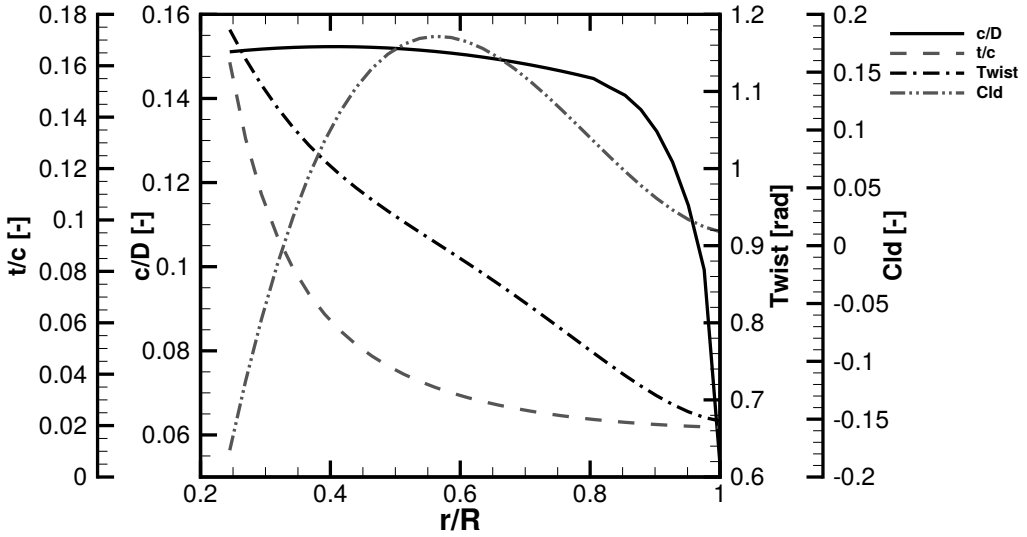

Fig. 2 *SR*2 *spanwise geometry.*

Table 2 *Fore and aft rotor setting angles.*

Configuration	$\beta_{1_{.75}}$ [^{o}]	$\beta_{2_{.75}}$ [^{o}]
Baseline	33.0	32.7
Fore-locked	83.2	37.3
Aft-locked	36.8	83.4

III. Computational Model

The Helicopter Multi Block (HMB3) solver [19, 20] was used to perform unsteady Reynolds Averaged Navier-Stokes (uRANS) CFD simulations. This was coupled to the Helicopter Ffowcs Williams-Hawkings (HFWH) code to compute the noise for each configuration.

A. Mesh Generation

To handle the relative motion of the rotating blade rows, the Chimera technique [21] has been used. The Chimera technique is an overlapping meshing strategy that allows for multiple non-matching grids to be used. For Chimera grids, the overlapping regions exchange field variables by interpolating between grid layers based on a defined hierarchy of grid levels. The Chimera technique allows for complex geometries to be broken down into smaller domains that can be easily meshed. Furthermore, in the current context, it allows for the rotor blades to be re-pitched without having to reconstruct the blade geometry and mesh. For the CROR simulations, the computational grid consists of the stationary background grid containing the spinner and far-field and $N_1 + N_2$ Chimera grids.

For the rotor grids, only a single rotor blade is meshed. For the fore row, this blade is re-pitched and copied to give the full blade count. For the aft row, the blade is mirrored about the y-axis before being re-pitched and copied to give the full blade count. The required setting angles were approximated using a CROR BEMT tool [18]. The current

implementation of the Chimera technique in the HMB solver does not allow solid bodies to intersect. Therefore, a small gap exists between the spinner and blade hub. As a result, this will produce non-physical flow features in this area. However, as the area near the hub is not highly loaded, we can neglect the acoustic contribution of this area without significantly affecting the overall noise levels. The rotor blade grid was created using a C-H topology. The grid was refined towards the blade surface, and the hub and tip gap regions to ensure $y^+ \leq 1$. Figure 3 shows the topology and mesh for a rotor blade at the mid-span position. Each Chimera grid comprised 86 blocks and ~6.6 million cells.

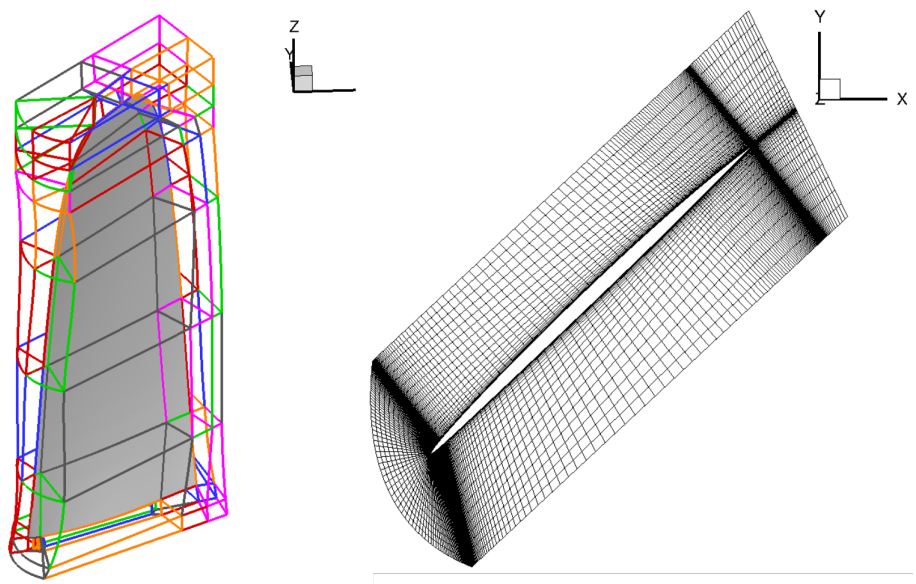

Fig. 3 *Blade topology and grid.*

For the spinner and background grids, the symmetry of the configuration is further exploited, and only a quarter of the domain is meshed. This is then copied and rotated to give the full spinner and background domain. An O-grid is employed in the azimuthal direction and an H-grid used in the meridional plane. The grid is extended 10R upstream, 15R downstream, and 6R in the radial direction, far enough to ensure no recirculation in the computational domain. The grid was refined in the rotor and near wake regions and coarsened towards the far-field in the axial and radial directions. Equally spaced cells were used around the azimuth. Refinement of the grid in the near-wall region of the spinner was used to ensure $y^+ \leq 1$. To simplify the grid, the spinner was extended far downstream. The quarter background grid consisted of 352 blocks and ~13 million cells. The entire computational domain consisted of 2,096 blocks and ~100 million cells.

Figure 4 shows the assembled surface grids. Orange represents the spinner surface; red and blue represent the fore and aft blade grids, respectively; the black outlines show the Chimera boundaries for each blade grid.

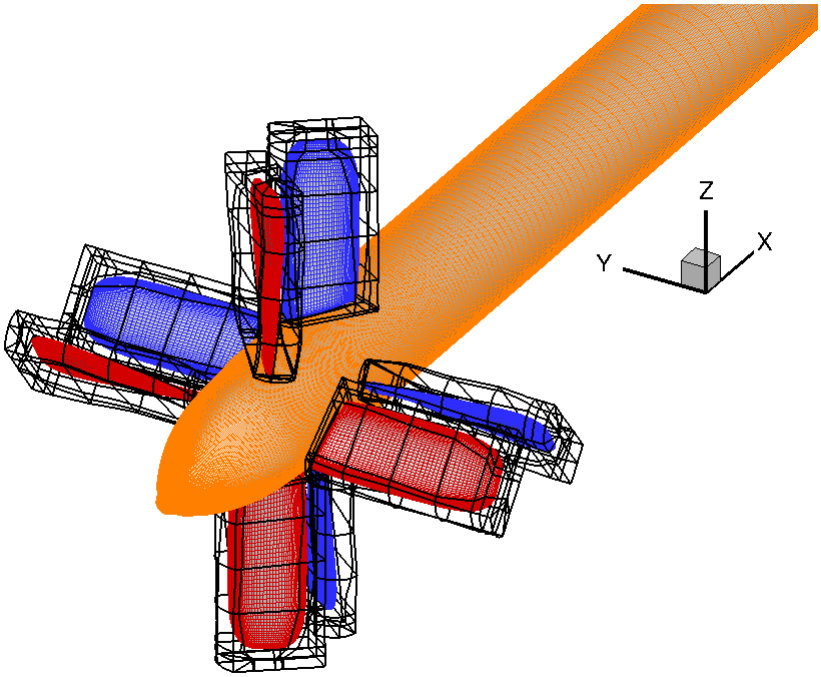

Fig. 4 *Assembled surface grids (every second cell shown).*

B. The HMB Solver and CFD Simulation

The HMB3 solver [19, 20] was used to perform the CFD computations throughout this work. HMB3 solves the uRANS equations in dimensionless, integral form using the arbitrary Lagrangian-Eulerian [22] formulation for time-dependent domains with moving boundaries:

$$\frac{\mathrm{d}}{\mathrm{d}t}\int_{\mathcal{V}(t)} \boldsymbol{W}\,\mathrm{d}\mathcal{V} + \int_{\partial\mathcal{V}(t)} (\boldsymbol{F}_i(\boldsymbol{W}) - \boldsymbol{F}_v(\boldsymbol{W}))\cdot\boldsymbol{n}\,\mathrm{d}S = \boldsymbol{S} \tag{1}$$

$\mathcal{V}(t)$ is the time-dependent control volume, with $\partial\mathcal{V}(t)$ its boundary; $\boldsymbol{W}$ is the vector of conservative variables, $[\rho, \rho u, \rho v, \rho w, \rho E]^T$; $\boldsymbol{F}_i$ and $\boldsymbol{F}_v$ are the inviscid and viscous fluxes respectively; $\boldsymbol{n}$ is the unit normal vector pointing outwards and $\boldsymbol{S}$ is the source term. Where a moving grid is employed, this source term is set to zero. Otherwise, this has a non-zero value, i.e. for steady rotor simulations, a fixed grid can be employed with source terms to account for inertial effects. HMB3 offers several uRANS turbulence models to close the viscous stress tensor, including the k-ω SST [23] model which was used throughout this work.

HMB3 discretises the Navier-Stokes equations using a cell-centred finite volume approach on a multi-block grid. This is done on a curvilinear coordinate system, and leads to the following set of equations to solve:

$$\frac{\mathrm{d}}{\mathrm{d}t}(\boldsymbol{W}_{i,j,k}\forall_{i,j,k}) + \boldsymbol{R}_{i,j,k} = 0 \tag{2}$$

$\boldsymbol{W}_{i,j,k}$ is the vector of conserved variables of each cell, with $\forbar{V}_{i,j,k}$ the cell volume; $\boldsymbol{R}_{i,j,k}$ is the vector of flux residuals.

Osher's upwind scheme [24] is used to evaluate convective fluxes. Second-order finite differencing is employed to discretise the viscous fluxes. The MUSCL variable extrapolation method [25] is used to provide second-order accuracy in space. A van Albada limiter [26] is used in areas of high-pressure gradients to remove spurious oscillations. An implicit dual time-stepping method is employed to perform time integration in order to achieve fast convergence. The resulting system of linear equations is solved using the generalised conjugate gradient method with a Block Incomplete Lower-Upper (BILU) factorisation [27] as a pre-conditioner. Multi-block grids are used for the HMB3 solver, and hence, allows for parallelisation and distribution of the calculation load over many processors.

For each configuration, in the initial stages of the simulation, the rotational speed is gradually increased from zero to the required speed over a single rotation. Furthermore, the first two revolutions use a temporal resolution of 360 steps per revolution. After the second revolution, as required by the acoustic criteria to ensure a sufficient frequency resolution, a temporal resolution of 720 steps per revolution (i.e. 0.5^o azimuthal steps) is used (see §V). At least 4 rotor rotations were required to obtain statistical time-invariance of the flow variables, after which flow-field data were recorded over a further complete rotor revolution. Simulations were carried out on the EPSRC Tier-2 National HPC facility, Cirrus, and the University of Manchester HPC Pool facility. Using 512-544 cores, the simulations took ~ 14 days (wall-time) to compute.

1. Solver Validation

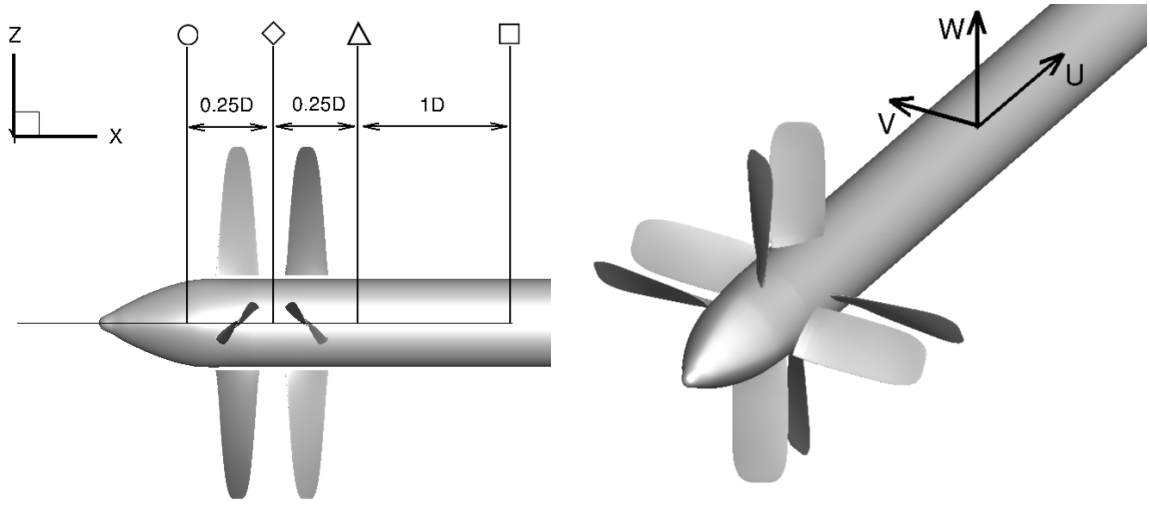

(a) *Location of velocimetry points/ CFD probe locations* (b) *Velocity components*

Fig. 5 *Location of probes and CROR reference frame.*

The HMB3 solver has been validated for a wide range of complex flow cases [19, 28, 29]; however, to ensure the

validity under the current case, the solver has been compared against available experimental data for a scale CROR. Dunham *et al.* [30] presented laser velocimetry measurements for a 0.409 m diameter, 4×4 CROR in the NASA Langley 4×7 wind tunnel. The quality of the reported data is not known. However, as the only source of available test data in the open literature (to the authors' knowledge), it is used here to validate the solver for this case. Three components of velocity are reported for a CROR at an advance ratio of $J = 1.21$ at a number of axial locations. Figure 5 shows the axial locations where velocity components have been recorded for a number of radial points. For the CFD simulation, numerical probes have been placed in the grid cell-centres nearest to those of the experiment.

Figure 6 compares the three components of mean velocity at each axial location reported by Dunham *et al.* [30] and those obtained using the HMB3 solver. Note: no upstream radial velocity was reported. Furthermore, whilst the data presented by Dunham *et al.* were time-averaged over 1-minute, the CFD data have been time-averaged over a single rotor revolution.

The comparisons show that the solver, having been trimmed to within 3.5% of the reported thrust coefficient, generally predicts the velocity profiles well. For the axial component, Figure 6(a), the acceleration of the flow is well captured. The maximum discrepancy with the experimental data is ~10%, found just downstream of the fore rotor. This would be expected to improve if the rotors were trimmed more closely to the reported thrust coefficient.

For the tangential and radial components, Figures 6(b) and 6(c) respectively, the profiles are also well captured. In particular, for each, the location of the tip vortices are well captured. However, there is a discrepancy in the value of the peak velocity deficit. This discrepancy may be due to differences in the locations of the probes, as this has been found to be quite sensitive to the resulting profiles.

The discrepancies observed may be further attributed to the unknown accuracy of the reported data. Furthermore, given the high rotation rate, the blades will likely have deformed from the original modelled geometry whilst running; therefore, this will affect the aerodynamic performance. Nevertheless, the HMB solver has been able to predict the reported data to a sufficient level of accuracy for this work.

C. The HFWH Code Aeroacoustic Simulations

The Helicopter Ffowcs Williams-Hawkings (HFWH) code was used to predict the CROR noise throughout this work. The HFWH code solves the Farassat 1A formulation [31] of the original Ffowcs Williams-Hawking equation [32]. The Farassat formulation is given by a summation of thickness and loading contributions:

$$p'(\boldsymbol{x}, t) = {p_L}'(\boldsymbol{x}, t) + {p_T}'(\boldsymbol{x}, t) \tag{3}$$

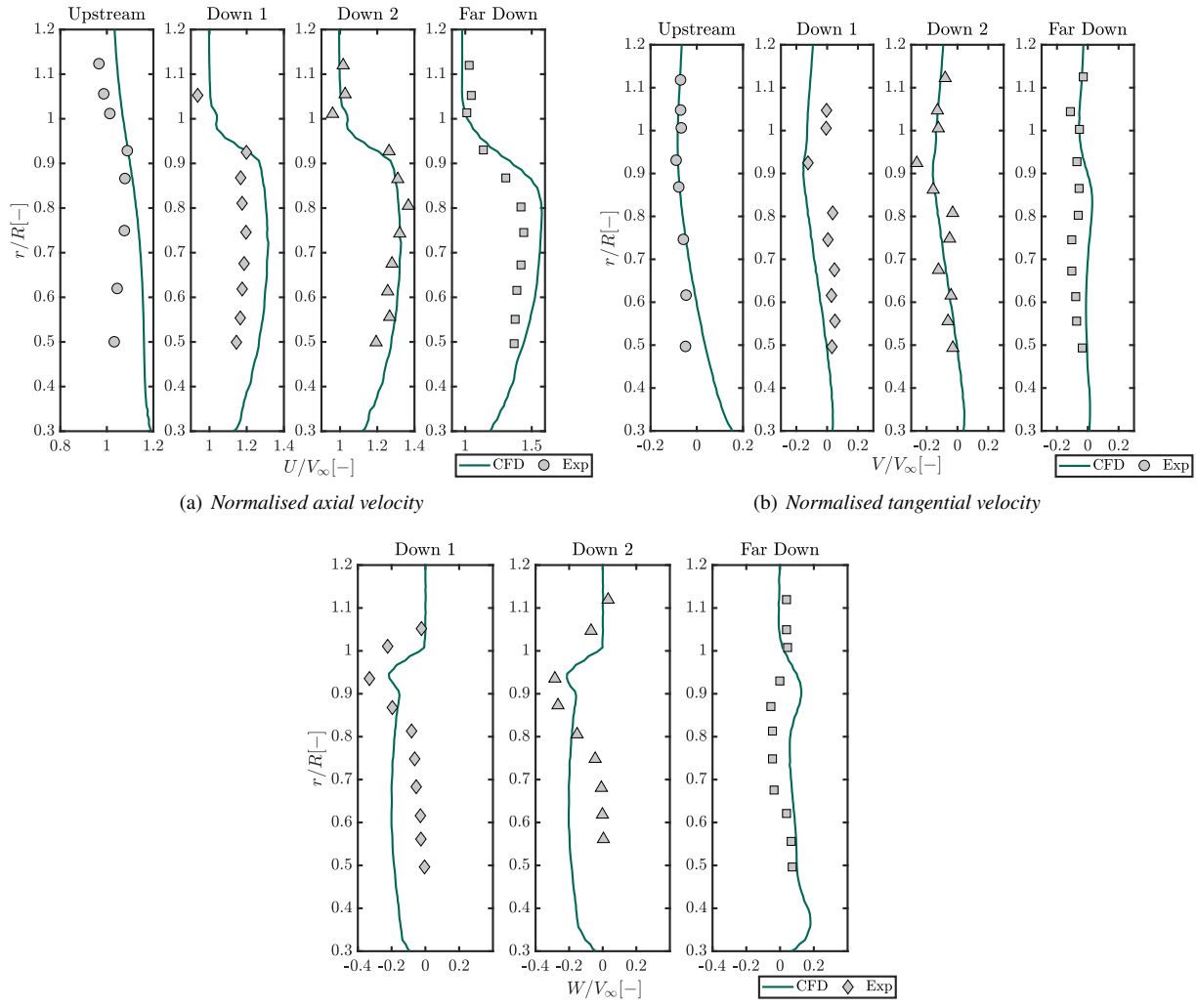

(a) *Normalised axial velocity*

(b) *Normalised tangential velocity*

(c) *Normalised radial velocity*

Fig. 6 *Comparison of experimental and computational CROR flowfield predictions.*

where,

$$4\pi {p_T}'(\boldsymbol{x},t) = \rho c_0 \int_{f=0} \left[\frac{\dot{M}_n}{\mathcal{R}(1-M_r)^2} + \frac{M_n \dot{M}_r}{\mathcal{R}(1-M_r)^3} \right]_{ret} \mathrm{d}S + \rho c_0 \int_{f=0} \left[\frac{c_0 M_n (M_r - M^2)}{\mathcal{R}^2 (1-M_r)^3} \right]_{ret} \mathrm{d}S \tag{4}$$

and

$$4\pi {p_L}'(\boldsymbol{x},t) = \int_{f=0} \left[\frac{\dot{p}_S \cos\Theta}{c_0 \mathcal{R}(1-M_r)^2} + \frac{\dot{M}_r p_S \cos\Theta}{\mathcal{R}(1-M_r)^3} \right]_{ret} \mathrm{d}S + \int_{f=0} \left[\frac{p_S(\cos\Theta - M_n)}{\mathcal{R}^2(1-M_r)^2} + \frac{p_S \cos\Theta (M_r - M^2)}{\mathcal{R}^2(1-M_r)^3} \right]_{ret} \mathrm{d}S \tag{5}$$

p_S is the blade surface pressure from the aerodynamic loading on the blade; M_r and M_n are the projection of the local Mach number, M, in the observer and normal directions respectively; Θ is the angle between the radiation and normal directions; $\mathcal{R}$ is the distance between source and observer. The $1/\mathcal{R}$ terms represent the far-field contribution whilst the $1/\mathcal{R}^2$ terms represent the near-field contributions.

The current implementation has neglected the quadrupole source. This has been justified as the tip Mach number remains relatively low in the present analysis. Additionally, we have neglected the broadband component. Although this has been shown to be important for CROR in some cases [33], a preliminary analysis with a low-order tool [34] suggested the tonal component was much more significant in the present case.

The implementation of the Farassat 1A formulation discretises the blade surface into panels. From the local panel velocities and surface pressures, the acoustic pressure can be calculated for each radial and chordwise position on the blade. The computed pressure represents the value that reaches the observer. The acoustic pressure of fore and aft rotors are computed independently with the HFWH code. The total contribution is obtained by summing the acoustic pressures of fore and aft rotors. Figure 7 shows a typical blade discretisation for the implementation of the HFWH code.

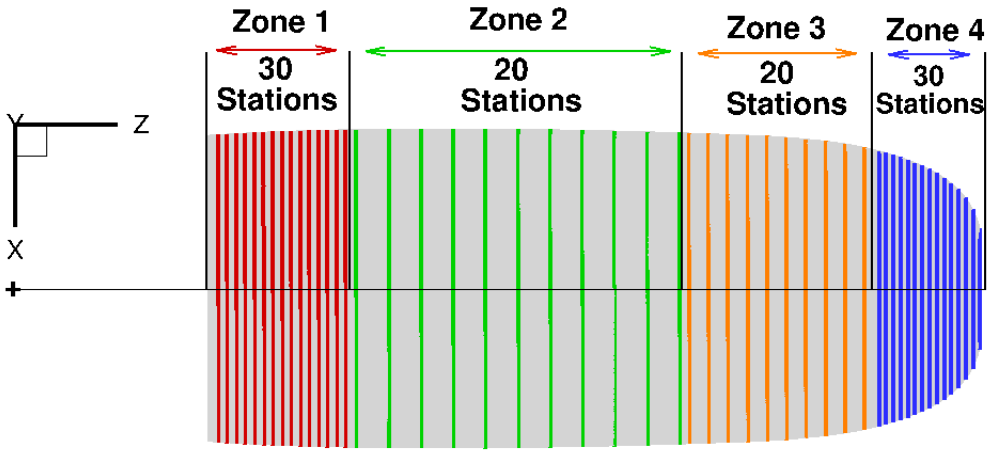

Fig. 7 *Blade discretisation for HFWH simulations (every second slice shown).*

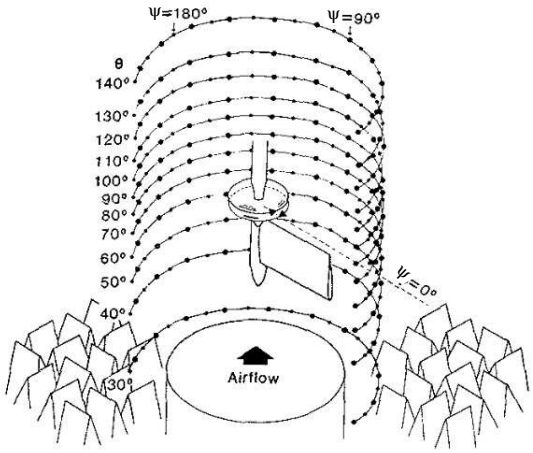

Fig. 8 *Microphone locations for HFWH validation, adapted from Ref.* [35].

1. Solver Validation

To validate the HFWH code, it is compared with experimental data for a 4×4 CROR. Block [35] presented directivity trends for a scale SR2 CROR up to the third harmonic. Both rotors rotated at an equal speed of 192 rev/s and were both 0.409 m in diameter. The CFD model replicated the test conditions assuming ISA sea-level conditions. A temporal resolution of 720 steps per rotation, i.e. 0.5^o steps were used. The HFWH analysis was performed for a number of numerical microphones used to replicate the azimuthal and polar directivities reported, Figure 8. The resulting sound pressure levels for the OASPL and first three harmonics were averaged over the azimuthal directivity. To match the reported data, this averaging was done according to:

$$\overline{SPL}(\theta, f) = 10\log\left(\frac{1}{n}\sum_{i=1}^{n} 10^{\frac{SPL(\theta,\psi_i,f)}{10}}\right) \tag{6}$$

where n is the number of azimuthal microphone positions. Figure 9 compares the OASPL and SPL of the first three harmonics reported by Block [35] and those obtained using the HFWH code at the reported microphone locations. The HFWH code has generally predicted the noise relatively well across the directivity for the OASPL and first three harmonics. For the OASPL and second harmonic of BPF, there is good agreement across the directivity, with only a slight discrepancy in the upstream directions (towards $\theta = 0°$). The first harmonic of BPF also shows good agreement, with a slight over-prediction for increasing polar angles away from 90°. The third harmonic shows the greatest discrepancy with the reported data. Good agreement is shown for higher polar angles. However, for polar angles less than 90° there is considerable disagreement. As the data has been averaged over the azimuth, it is difficult to isolate discrepancies for a particular polar angle. However, the discrepancies shown appear for polar angles away from the overhead position, where the interaction component becomes more significant. Therefore, the observed discrepancies

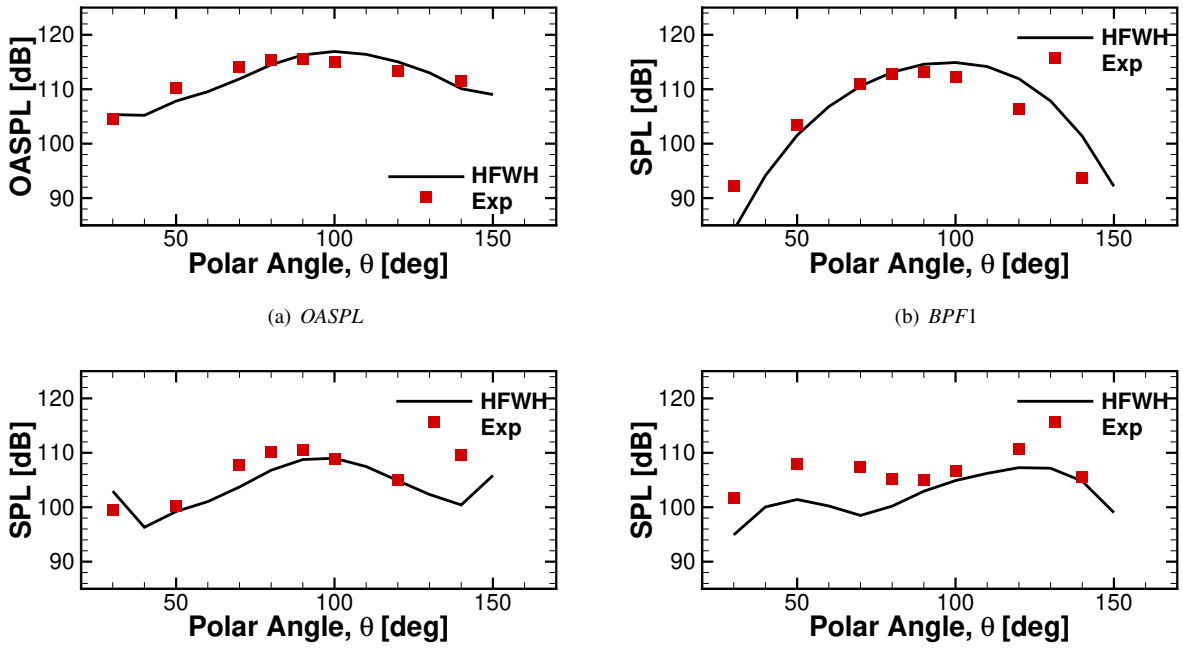

(a) *OASPL*

(b) *BPF*1

(c) *BPF*2

(d) *BPF*3

Fig. 9 *Comparison of experimental and numerical noise levels at the reported polar microphone locations.*

may result from the resolution of the up- and downstream interaction between blade rows. Nonetheless, the sound levels are predicted to a sufficient level of accuracy for the computations in this work.

IV. Aerodynamic Analysis

The HMB solver was used to perform the CFD computations of each CROR configuration. For each case, the k-ω SST turbulence closure [23] was used. Simulations required at least four rotations to give time-invariance of the flow variables. A final rotation was then computed, from which the data was extracted. Acoustic criteria required a time step of 0.5^o, for which blade surface pressure was extracted at each time step.

The locked-rotor concept is proposed to reduce CROR noise in the terminal area. However, configurations with a locked blade row must also provide sufficient aerodynamic performance such that the aircraft can perform take-off and climb-out manoeuvres safely and efficiently. This section proceeds by assessing the aerodynamics of each configuration to ensure this performance can be met. This is followed by a focus on the noise generating mechanisms.

The analysis was carried out to simulate take-off conditions, i.e. the terminal area for noise validation. This resulted in a required thrust of 6 kN at $M = 0.2$. This thrust was achieved for all configurations by adjusting the blade setting angles with the rotational speed constant for all cases. The blade setting angles for each configuration were computed from a CROR aerodynamic tool [18], Table 2. Table 3 presents the computed thrust for each rotor for each configuration, as well as the difference relative to the 6 kN target thrust. Note: for the inoperative configurations, the operative rotor

has to meet the required thrust in addition to overcoming the drag (negative thrust) produced by the locked row. Table 3

Table 3 *Computed thrust for each configuration. Target thrust = 6 kN.*

Case	T_1 $[kN]$	T_2 $[kN]$	$T_1 + T_2$ $[kN]$	Δ_{Target} [%]
Baseline	3.06	3.05	6.12	+1.90
Fore-locked	−0.195	6.34	6.14	+2.37
Aft-locked	5.94	−0.0961	5.85	−2.57

shows that the baseline CROR has an almost equal thrust loading between rotors (i.e. $T_1/T_2 \sim 1$), as specified by the CROR aerodynamic tool. Furthermore, both locked rows produce relatively low levels of negative thrust, whilst the operative rows produce sufficient levels to meet the required thrust. However, whilst the aft-locked configuration produces slightly less thrust than required, this is by only a small margin. This could be improved by increasing the blade setting angle. Overall, each configuration provides sufficiently comparable thrust levels to the target thrust to allow a fair comparison of the resulting noise levels.

For the inoperative configurations, whilst the operative row is trimmed to deliver the required thrust, the locked row is trimmed to minimise torque. Table 4 presents the computed torque from each rotor for each configuration. The baseline configuration presents an almost equally balanced torque ratio. On the other hand, the fore rotor of

Table 4 *Computed torque and efficiency of each configuration.*

Case	Q_1 [kNm]	Q_2 [kNm]	η [%]
Baseline	−2.50	2.49	79.4
Fore-locked	0.233	5.55	73.9
Aft-locked	−5.22	1.55	72.5

the fore-locked configuration has been successfully trimmed to a sufficiently small torque level. The aft rotor of the fore-locked configuration produces a relatively high torque reaction. However, this is comparable to the absolute sum of the baseline configuration. The fore rotor of the aft-locked configuration produces a similar torque reaction. However, unlike the locked row of the fore-locked configuration, the locked row of the aft-locked configuration produces a significant torque reaction. Nonetheless, this torque reaction may be reduced by suitable adjustment of the blade setting angle. However, this torque will have to be compromised with the resulting negative thrust levels. The resultant high torque value for the locked row may also present a limitation of the CROR BEMT tool in predicting loads of a locked rotor. Despite the torque reaction being greater for both inoperative configurations, the values are still well within the limits of the engine*.

Table 4 also presents the computed efficiency for each configuration, where the efficiency was computed according

*Of the aircraft simulated for the thrust requirements.

to:

$$\eta = \frac{V_\infty (T_1 + T_2)}{\Omega_1 Q_1 + \Omega_2 Q_2} \tag{7}$$

Table 4 shows that the baseline CROR produces a high efficiency, particularly for this take-off case. Both inoperative configurations produce the required thrust less efficiently, with efficiency reductions of 5.5% and 6.9% for the fore-locked and aft-locked configurations, respectively.

The resulting efficiency has shown that locking a blade row does not significantly impact the ability of the rotors to deliver this thrust. In fact, the thrust is still delivered relatively efficiently despite the locked row. It is worth commenting briefly on the description of the efficiency used above. Equation (7) is the standard equation used to define propeller efficiency [36]. However, when a blade row is locked ($\Omega = 0$), the effect of the torque of the inoperative row on the propulsion system is not accounted for within the description of efficiency. Therefore, the efficiency alone cannot describe the performance of the CROR with a locked blade row.

The interaction of the fore wake with the rear row, in addition to the up and downstream potential interactions, give rise to unsteady loading, and hence unsteady acoustic sources from both CROR blade rows. Figure 10 shows the periodic loading for each configuration over a single rotation. The fore and aft rotors of the baseline CROR are

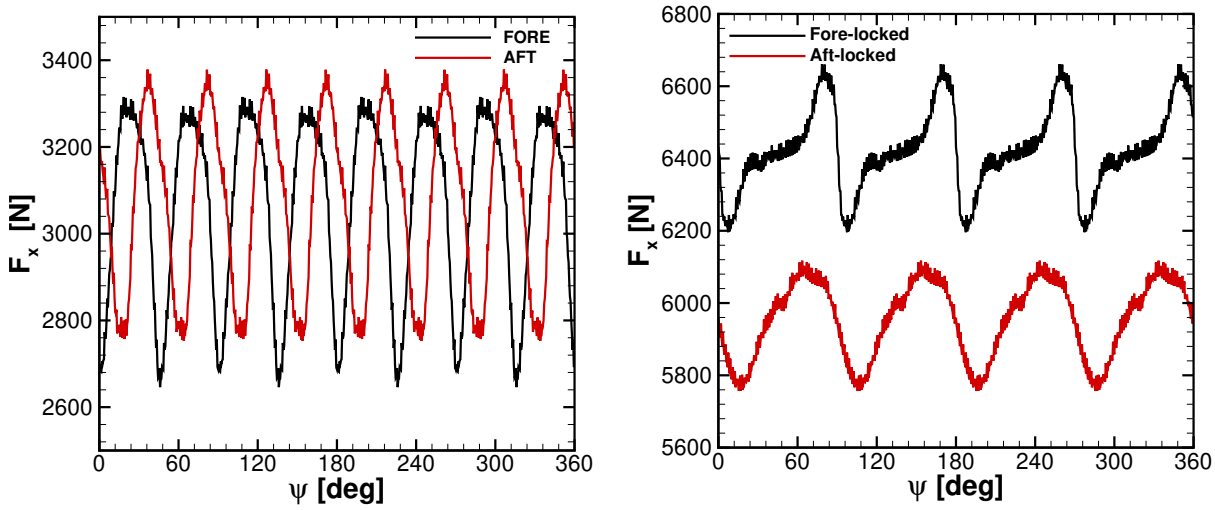

(a) *Operative CROR*

(b) *Operative rotor loads for locked-row configurations*

Fig. 10 *Azimuthal axial forces for each configuration.*

characterised by an 8-peak sinusoidal response (equal to $N_1 + N_2$) around a mean value. This behaviour is a result of the mutual interaction between the blade rows. The fore rotor shows a minimum starting at $\psi = 0^o$ and at intervals of $\Delta\psi = 45^o$, i.e. the location of overlap between the blade rows. The aft row shows similar behaviour to the fore with a phase shift of around $\Delta\psi = 15.5^o$. This change in phase is caused by the interaction with the wake from the fore rotor, which will meet the aft rotor at some time later corresponding to this phase shift. Fore and aft rotors show similar

amplitudes around their mean values, highlighting the equal importance of up- and downstream interactions.

As both inoperative configurations interact with a stationary blade row, interactions will only occur N times, where N is the blade count of the stationary row. Therefore, Figure 10 shows that both fore- and aft-locked loads are characterised by a 4-peak response around a mean value. The aft-locked configuration shows a sinusoidal response around a mean value. On the other hand, the fore-locked configuration shows a more impulsive response. The response is characterised by a sinusoidal peak followed by an almost constant value before the next sinusoidal peak. This response reflects the behaviour of the interaction. With the fore rotor locked, the wake and tip vortices will travel in the axial direction only. This behaviour will result in an intermittent interaction with the operative rear row. This is in contrast to the baseline configuration, where the interaction will be more continuous. The difference in mean loading level between both inoperative configurations is due to the differences in the blade setting positions.

The interactions described will result in increased noise levels across the directivity when compared to an isolated rotor. The wake interaction can contribute significantly to the high noise emissions [37], particularly at take-off conditions. Figure 11 presents the wake profiles for each configuration at a $0.75R$ position behind the fore rotor, measured over a single rotation. All configurations are characterised by a periodic response around a mean value.

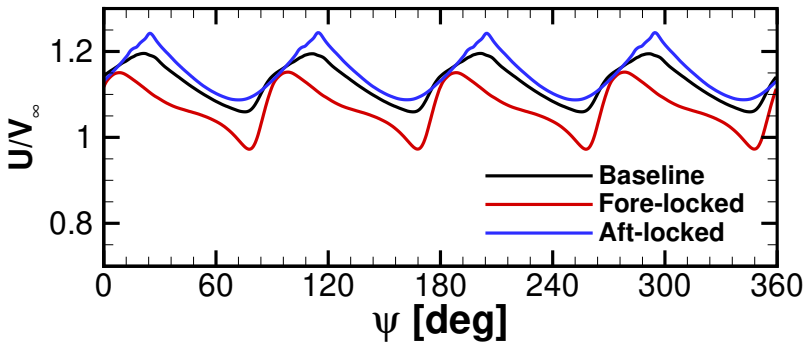

Fig. 11 *Wake profiles around azimuth for each configuration.*

The period of each corresponds to the blade count, here four. Both the baseline and aft-locked configurations (i.e. configurations with a running fore rotor) show similar responses. However, the aft-locked shows a greater amplitude due to the higher loading relative to the baseline configuration. The fore-locked configuration shows an interesting wake pattern. The profile shown demonstrates the effect and significance of the upstream interactions. In all cases, the wake profiles will interact with the aft rotor. For the baseline and fore-locked configurations, this may be more significant as the aft rotor is operative in both cases.

Without clipping the aft rotor, the tip vortex of the fore rotor will impinge on the aft rotor. This presents a significant noise source [38] — tip vortex interaction noise. To visualise the tip vortices, Figure 12 shows iso-surfaces of Q-criterion [39] for each configuration, where $Q = 0.2$ for each. Due to the reduced loading, the baseline configuration

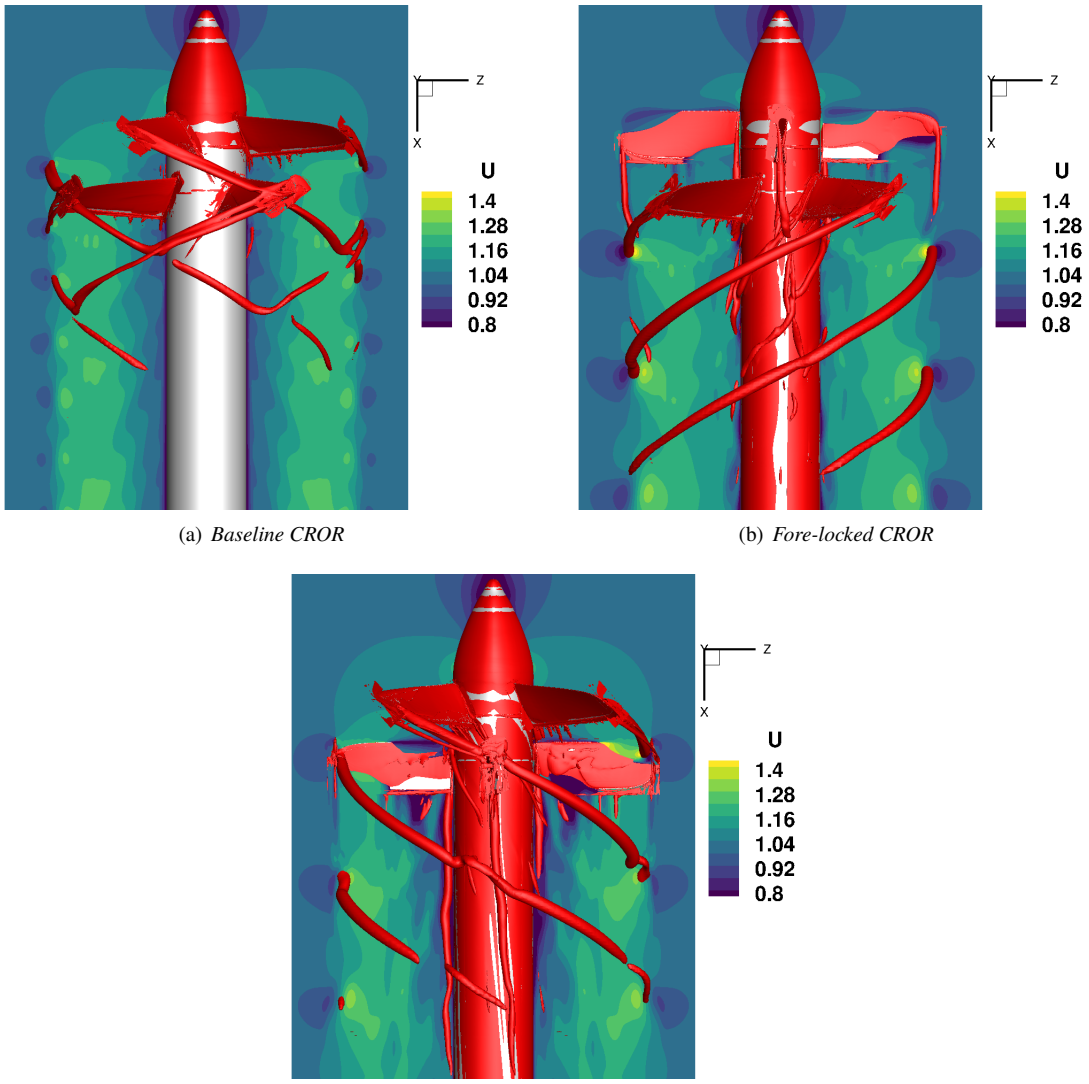

(a) *Baseline CROR*

(b) *Fore-locked CROR*

(c) *Aft-locked CROR*

Fig. 12 *Contours of axial velocity with iso-surfaces of Q-criterion, $Q = 0.2$ for each configuration.*

has much weaker tip vortices than both fore- and aft-locked configurations. However, these tip vortices are impacting on a rotating blade row and will, therefore, have a significant impact on the resulting noise levels. The fore-locked configuration shows vortical structures emanating from both fore and aft rotors. The tip vortex from the locked fore blade row will interact with the rotating rear row and will give rise to tip vortex interaction noise. The tip vortex from the operative rear row is much stronger. However, it will not give rise to tip vortex interaction noise. The aft-locked configuration has a similarly strong tip vortex. However, this tip vortex will impinge on a locked blade row and therefore, should have no serious impact on the noise of the stationary row.

V. Aeroacoustic Analysis

Aeroacoustic simulations were carried out for all three configurations. To perform the aeroacoustic analysis, the HMB solver was coupled to the HFWH code to compute the far-field noise. A time resolution resulting from 0.5^o time steps was used for the simulations. This results from a compromise of computational cost, requirements of the Chimera implementation and sufficient frequency resolution. In the present case, the maximum resolved frequency is $\sim$ 6 kHz. Blade surface pressures were extracted at each time step over a complete rotation to compute the resulting noise at a number of observer locations. For each configuration, both polar and azimuthal directivities were investigated. For the polar directivity, an array of numerical microphones were placed 1,000 feet (304.8 m) below the CROR to simulate a constant altitude flyover. For the azimuthal directivity, a ring of 360 numerical microphones was placed around the CROR at the midpoint between fore and aft rotors. Figure 13 demonstrates the locations of the numerical microphones. The analysis was carried out primarily using the A-weighted Sound Pressure Level (SPL), in line with general aviation aircraft noise certification [14].

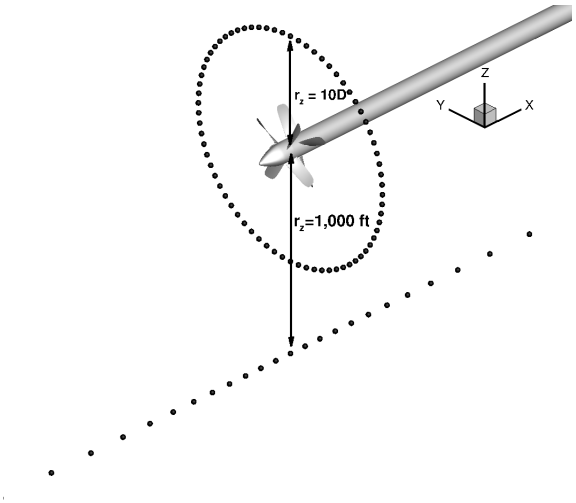

Fig. 13 *Microphone locations for aeroacoustic analysis* (*note*: *positions not to scale and not every point shown*).

The aim of locking a blade component is to reduce CROR noise in the terminal area. Figure 14 compares the computed noise levels of each configuration for a 1,000 feet (304.8 m) simulated flyover at the specified microphone locations.

Locking either fore or aft rotor, whilst maintaining the required thrust, is shown to produce less noise over the whole flyover compared to the baseline configuration. The aft-locked configuration produces the lowest noise levels across the directivity, with the fore-locked configuration showing higher levels in the up- and downstream directions. It is interesting to note that for all configurations there are high noise levels across the whole directivity, and in particular towards the axis of rotation. This is characteristic of CROR noise and highlights the importance of the interactions. Furthermore, this suggests that the interaction between locked and running rotors is also important for the locked-rotor

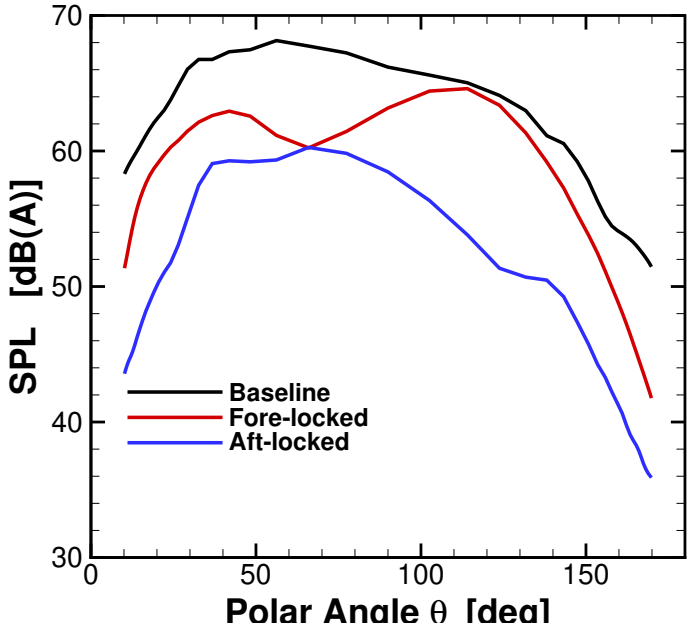

Fig. 14 *A-weighted SPL computed for each configuration.*

configurations.

Table 5 presents the peak noise levels in terms of maximum A-weighted SPL ($LA_{\max}$) for each configuration. The Effective Perceived Noise Level (EPNL) is an integral metric that accounts for intensity and the duration of a noise source. Therefore, due to the highly directive nature and the unique spectral response of CROR noise, the $EPNL$ metric is perhaps more suited for comparing CROR noise. To this end, Table 5 also presents the computed EPNL for the flyover. Table 5 shows again that the noise is greatly reduced when a CROR blade row is locked. Compared to the

Table 5 *Noise levels for each configuration.*

Configuration	EPNL [dB]	$LA_{\max}$ [dBA]
Baseline	66.7	68.1
Fore-locked	59.7	64.6
Aft-locked	54.7	60.2

baseline configuration, noise reductions of 3.5 dBA and 7.9 dBA can be achieved when locking either fore or aft rotors, respectively. Using the EPNL metric, this results in reductions of 7 EPNLdB and 12 EPNLdB for fore- and aft-locked configurations respectively. This is a significant noise reduction, all whilst exploiting the high efficiency of the CROR in the cruise segment. The aft-locked configuration shows the greatest noise reduction with around a further 4.4 dBA (5 EPNLdB) over the fore-locked configuration. In addition to the slightly lower loading (Table 3), this reduction results from the stronger interaction components in the fore-locked configuration, caused by the operative rotor cutting through

the wake of the stationary fore blades.

To proceed, we must further investigate the noise components from each configuration to identify the sources that result in these noise reductions. Figure 15 shows the noise components for the baseline configuration.

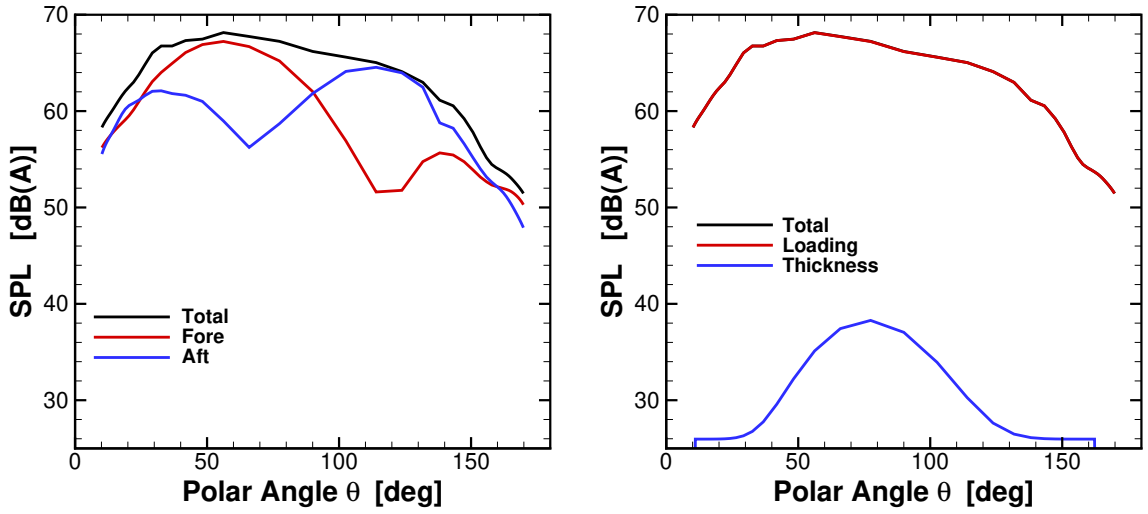

(a) *Fore and aft rotor contributions*

(b) *Thickness and loading contributions*

Fig. 15 *Noise components of the baseline configuration.*

Figure 15(a) shows the strong influence of the interactions for both fore and aft rotors. The upstream interactions result in peak levels of the fore rotor in the upstream directions. On the other hand, the downstream interactions result in peak levels in the downstream direction for the aft rotor. Due to the equal rotational speeds and blade counts, it is not possible to extract and study the interaction components further. However, the equal loading for both rotors would suggest comparable self-noise between fore and aft rotors. Therefore, the observed trends will result from the interaction between blade rows. As a result, the higher peak noise of the fore rotor suggests stronger upstream interactions.

Figure 15(b) compares the loading and thickness contributions of the baseline configuration. Over the whole directivity, the loading component dominates, with the thickness component making little contribution to the overall noise. This is expected for the given flight condition. However, during cruise conditions, the thickness component will become more significant as the relative blade velocity increases. The dominance of the loading component was observed for all three CROR configurations studied.

Figure 16 compares the contribution to the total noise from each rotor for both inoperative configurations. For the fore-locked configuration, the operative rotor dominates over most of the directivity. However, near the rotor plane, the locked component makes a significant contribution to the total noise. The high levels of the locked rotor highlight the effect of the wake interactions from the upstream stationary row.

For the aft-locked configuration, Figure 16(b) demonstrates that the locked rotor makes a more significant contribution to the total noise. This results from the use of the A-weighting. When comparing both rotors without A-weighting, the

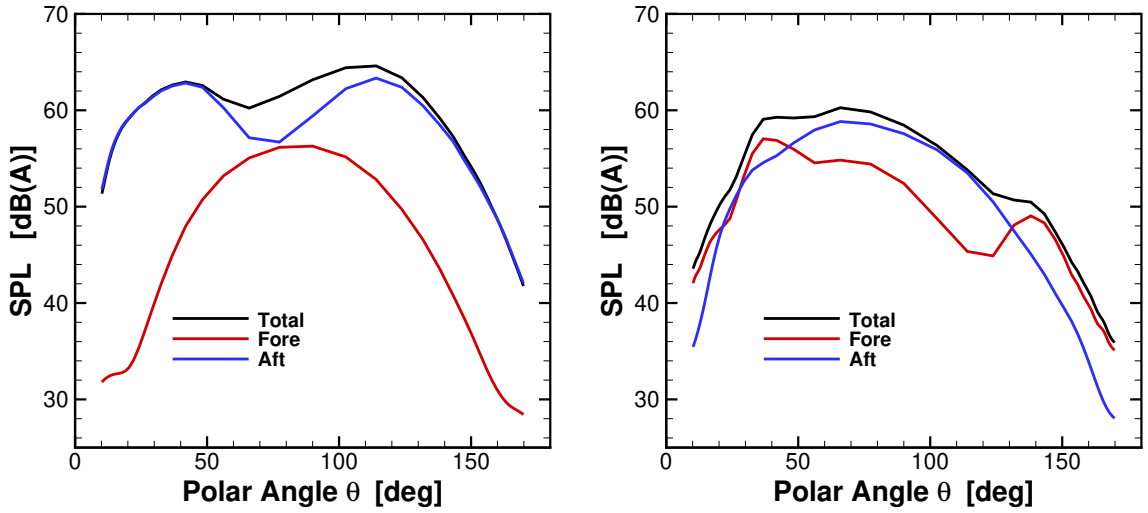

(a) *Fore-locked CROR* (b) *Aft-locked CROR*

Fig. 16 *Rotor noise contributions for fore- and aft-locked configurations.*

operative fore rotor had a much higher noise level than the locked aft rotor. In fact, the fore rotor dominated over the whole directivity, with the locked rotor making an insignificant contribution to the total noise. When the A-weighting is applied, the noise of the fore rotor is reduced considerably. On the other hand, the noise of the locked rotor was found to be significant at higher frequencies and therefore not so significantly impacted by the A-weighting. This results in a comparable noise level between the two rotors. Nonetheless, the significant levels of the locked rotor again show the importance of the contribution from the locked rotor.

The high noise levels of the locked rotor result from interaction with the wake from the operative rotor. The peak noise levels of the locked rotor are shown to be higher for the aft-locked configuration. Conversely, the fore-locked configuration shows the highest levels for the operative rotor between the two configurations. Therefore, the downstream interactions appear more significant for the locked-rotor configurations.

Figure 17 compares the azimuthal directivity of each configuration. Numerical microphones are located on a ring 10 diameters from the centre of rotation at the mid-point between both rotors, Figure 13. The values shown represent those computed at the microphone location. Figure 17 shows that the baseline configuration has the greatest noise levels over most azimuth angles. There are a number of locations where the fore-locked configuration has a greater noise level than the baseline configuration. The fore-locked configuration shows a 4-peak pattern with the peaks corresponding to the locations of increased noise level relative to the baseline. The aft-locked configuration shows the lowest noise levels throughout all azimuth angles.

To investigate the azimuthal directivities further, Figure 18 compares the contribution of each rotor for each CROR configuration. Note that the SPL metric has been used to retain some of the distinct features in this case. Additionally, the

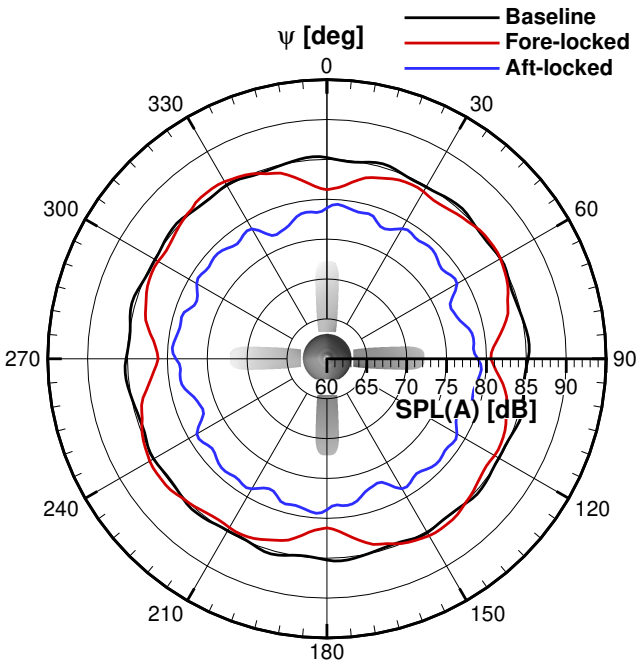

Fig. 17 *Azimuthal directivity of each configuration.*

scale is adjusted for each configuration to highlight these features. Considering the baseline configuration, Figure 18(a) shows that the fore rotor dominates over all azimuth angles. Both rotors show an 8-peak pattern around the azimuth. This behaviour results from the simultaneous blade passage that occurs due to the equal blade count and rotational speeds of fore and aft rotors. The aft rotor has a peak level at the origin and subsequently every 45°. The fore rotor has a peak at around 45° and subsequently every 45°. These correspond to the peak loading levels shown in Figure 10.

Considering the fore-locked configuration, Figure 18(b), the operative rotor contributes most significantly to the total noise. The locked rotor only has an impact on the total noise at its peak levels. The locked fore rotor shows an interesting 8-peak profile. The operative aft rotor also has an 8-peak profile. However, this shape is not clearly observable from the figure. These profiles demonstrate the importance of the aerodynamic interaction between both rotors. Also observed is the fact that at some azimuthal locations, the fore-locked configurations has a higher noise level than the baseline configuration.

The locked rotor of the aft-locked configuration, Figure 18(c), is shown to have a negligible impact on the total noise across all angles. The wake and downstream potential interactions from the operative fore rotor result in an 8-peak profile for the aft rotor. On the other hand, the fore rotor demonstrates a 4-peak profile. However, this feature is not easily observed in the current figure. This profile demonstrates the weaker impact of the interactions from the aft rotor.

We now consider the frequency response for all configurations. Figure 19 shows the SPL for the first ten harmonics for all three configurations at the overhead position of the flyover ($\theta = 90^o$). Figure 19 shows that all configurations share a similar SPL at the fundamental harmonic, indicating a similar level of self-noise between configurations. Despite

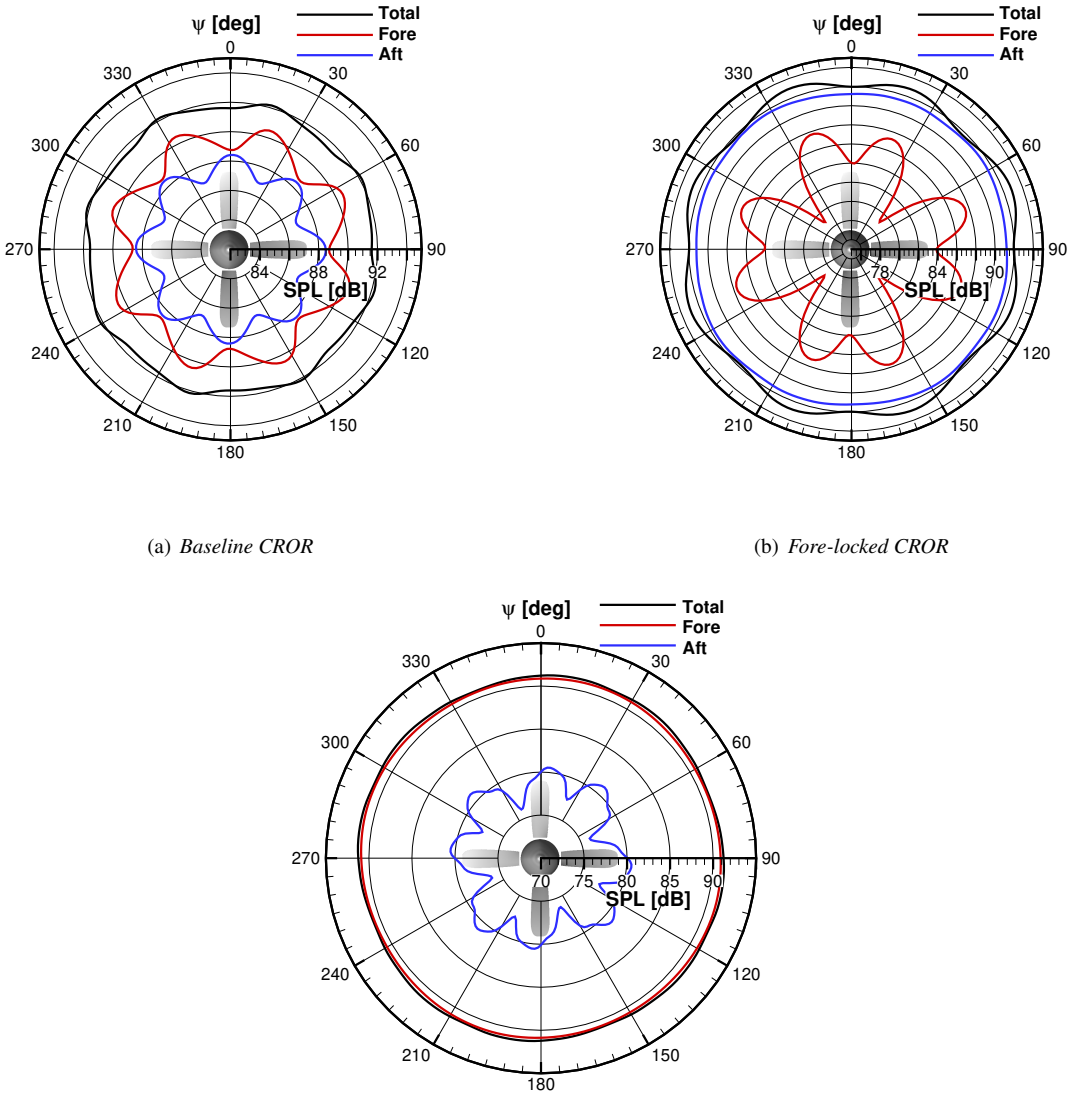

(a) *Baseline CROR*

(b) *Fore-locked CROR*

(c) *Aft-locked CROR*

Fig. 18 *Azimuthal directivity of rotor components for each configuration.*

the reduced loading, the baseline configuration shows a similar level due to the addition of fore and aft signals (which will constructively add due to equal blade counts and tip speeds). Examining the higher harmonic terms gives insight into the previously observed trends. The baseline configurations show high SPL levels across all harmonics. This is characteristic of CROR noise and is caused by the unsteady aerodynamic interaction and the acoustic interaction between rotors.

Considering the inoperative configurations, Figure 19 shows that the SPL of aft-locked configuration generally decreases for increasing harmonic. However, this is not a rapid reduction in SPL. Further, a number of harmonics show increased levels compared to that of a lower harmonic. These increased levels result from the contributions from the

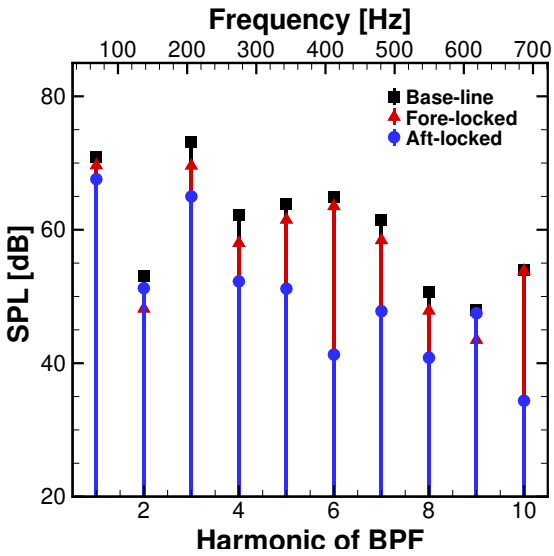

Fig. 19 *Harmonic components of the noise for all configurations.*

locked rotor. The fore-locked configuration generally shows an increased SPL compared to the aft-locked configuration. This increase is indicative of the stronger interactions for the fore-locked configuration. These responses highlight the importance of the aerodynamic interactions for the inoperative configurations.

Given the similar SPL levels of all configurations at the fundamental harmonic, the differences in peak noise levels must arise due to the higher frequency components. The increased noise levels at higher frequencies (as opposed to a rapid decay seen for isolated rotors) are due to the interactions between fore and aft blade rows. In particular, this becomes important for directivities approaching the axis of rotation. Therefore, the increased noise levels of the baseline configuration are due to the stronger interaction between blade rows. Whilst these also exist for the inoperative configurations, we can conclude that the increase in self-noise of a single rotor is less significant than the reduction in interaction noise that results.

The locking of a CROR blade row has shown reduced noise levels compared to the baseline CROR. Noise reductions are observed when using both SPL(A) and EPNL metrics. Furthermore, noise reductions were observed over all polar directivity angles. The azimuthal directivities showed profiles characteristic of the unsteady interaction between CROR blade rows of equal blade count. The aft-locked configuration showed the lowest noise levels across all angles. The baseline configuration generally showed the highest levels. However, there were a number of locations where noise levels of the fore-locked configuration was greater than the baseline. Comparisons of the frequency content showed that all configurations were affected by the mutual interactions between blade rows resulting in an increase in SPL for some increased harmonics. Comparing both inoperative configurations, the reduced interactions of the aft-locked configurations showed noise reductions in comparison to the fore-locked configuration. These noise reductions come at the cost of a small, but not limiting efficiency penalty. Therefore, locking a blade row can be used to reduce CROR noise.

Future work should consider a more multidisciplinary approach, confirming the installation of this multi-configuration CROR concept. Furthermore, the current baseline design may not be suitable in practice due to the disadvantages of equal blade count designs. Therefore, a more optimal design of different blade count should be considered in future.

VI. Conclusions

A coupled CFD-CAA numerical analysis has been performed to investigate the viability of a novel variable configuration CROR concept aimed at reducing noise. In particular, it is proposed to lock either fore or aft rotor during take-off, whilst both rotors are operated at their design point at cruise to take advantage of the high propulsive efficiency of CROR.

The aerodynamic analysis of each configuration confirmed the ability of the CROR to deliver the required take-off thrust whilst one blade row is locked. For both inoperative configurations, this thrust was found to be delivered with a 5.5% and 6.9% efficiency penalty relative to the baseline CROR for fore- and aft-locked configurations, respectively. Additionally, the aerodynamic analysis highlighted the equal importance of both up- and downstream interactions.

The analysis demonstrated the potential of the locked-rotor concept to reduce CROR noise through a reduction of the interaction component. However, the locked rotor was found to make a significant contribution to the total noise at a number of polar angles for both configurations. Nonetheless, for both inoperative configurations, noise reductions were observed for peak levels, as well as over a range of polar observer angles. From the simulated flyover, noise reductions of 3.5 dBA (7 EPNLdB) and 7.9 dBA (12 EPNLdB) were found for fore- and aft-locked configuration, respectively.

Considering the azimuthal directivities at the mid-plane between both rotors, all configurations demonstrated a behaviour characteristic of their unsteady loading. At a number of azimuthal locations, the fore-locked configuration demonstrated increased noise levels relative to the baseline. However, the aft-locked configuration was shown to have the lowest noise for all azimuth angles.

Analysis of the frequency components at the overhead position showed that all configurations had a similar level of self-noise. Additionally, all configurations were affected by increased SPL at increased harmonics, highlighting the importance of the interactions for all configurations.

The results showed that both inoperative configurations offered noise reductions, with the aft-locked configuration demonstrating the greatest reductions in terms of noise. However, this reduction came at the cost of a slightly larger penalty in propulsive efficiency. Nonetheless, given the increased noise levels of the fore-locked configuration at some locations, the aft-locked is more favourable. The baseline design considered in the analysis has a number of features that are less advantageous for low-noise, e.g. equal blade count and rotational speed and no clipping. Future work should, therefore, consider a more optimal design to investigate the concept. A design optimised for locked operation in the terminal area may prove the greatest noise reductions whilst alleviating the aerodynamic impact of the locked rotor. The present work has not accounted for broadband or installation effects which must be considered in future work.

Furthermore, the present preliminary analysis should be further verified to prove the viability of the proposed concepts.

The observed noise reductions show that the locked-blade concept may be useful for reducing CROR noise in the terminal area. The analysis carried out would allow for general aviation aircraft to operate with low community impact in take-off and climb-out, whilst maintaining high efficiency in cruise.

Funding Sources

This research is supported by a private sponsorship (Mr Mike Newton) and a UK Research Council Grant EP/S010092/1 (Methods and Experiments for Novel Rotorcraft).

Acknowledgments

The authors would like to acknowledge the use of the Cirrus UK National Tier-2 HPC Service at EPCC (http://www.cirrus.ac.uk) funded by the University of Edinburgh and EPSRC (EP/P020267/1). The authors would also like to acknowledge the assistance given by Research IT, and the use of The HPC Pool funded by the Research Lifecycle Programme at The University of Manchester.

References

[1] Van Zante, D. E., "Progress in Open Rotor Research: A U.S. Perspective," *ASME Turbo Expo 2015*, Montréal, Canada, 2015, pp. 1–14. https://doi.org/10.1115/GT2015-42203.

[2] Weckmüller, C., and Guérin, S., "On the influence of trailing-edge serrations on open-rotor tonal noise," *18th AIAA/CEAS Aeroacoustics Conference*, 2012. https://doi.org/10.2514/6.2012-2124.

[3] Jaron, R., Moreau, A., Guérin, S., and Schnell, R., "Optimization of trailing-edge serrations to reduce open-rotor tonal interaction noise," *Journal of Fluids Engineering, Transactions of the ASME*, Vol. 140, No. 2, 2018, pp. 1–8. https://doi.org/10.1115/1.4037981.

[4] Delattre, G., and Falissard, F., "Aerodynamic and acoustic impacts of a single protuberance placed on the leading edge of the front blades of an open rotor," *48th International Symposium of Applied Aerodynamics of Small Bodies and Details*, 2013.

[5] Delattre, G., Falissard, F., Vion, L., and Jacquin, L., "Open rotor interaction noise reduction through front rotor wake modification," *International Journal of Aeroacoustics*, Vol. 15, No. 1-2, 2016, pp. 207–227. https://doi.org/10.1177/1475472X16643461.

[6] Khalid, S. A., Wojno, J. P., Breeze-Stringfellow, A., Lurie, D. P., Wood, T. H., Ramakrishnan, K., and Paliath, U., "Open rotor designs for low noise and high efficiency," *Proceedings of the ASME Turbo Expo*, Vol. 6 C, 2013, pp. 1–14. https://doi.org/10.1115/GT2013-94736.

[7] Akkermans, R. A. D., Stuermer, A., and Delfs, J. W., "Assessment of Front-Rotor Trailing-Edge-Blowing for the Reduction of Open Rotor Noise Emissions," *19th AIAA/CEAS Aeroacoustics Conference*, 2013. https://doi.org/10.2514/6.2013-2200.

[8] Akkermans, R. A., Stuermer, A. W., and Delfs, J., "Active Flow Control for Interaction Noise Reduction of Contra-Rotating Open Rotors," *49th AIAA/ASME/SAE/ASEE Joint Propulsion Conference*, American Institute of Aeronautics and Astronautics, Reston, Virginia, 2013. https://doi.org/10.2514/6.2013-3799.

[9] Stürmer, A., and Akkermans, R. A. D., "Multidisciplinary analysis of CROR propulsion systems: DLR activities in the JTI SFWA project," *CEAS Aeronautical Journal*, Vol. 5, No. 3, 2014, pp. 265–277. https://doi.org/10.1007/s13272-014-0105-4.

[10] Stuermer, A., Akkermans, R. A. D., and Delfs, J. W., "Assessment of front rotor trailing edge blowing for the reduction of open rotor interaction noise," *Notes on Numerical Fluid Mechanics and Multidisciplinary Design*, Vol. 124, 2014, pp. 609–618. https://doi.org/10.1007/978-3-319-03158-3_62.

[11] Akkermans, R. A. D., Stuermer, A., and Delfs, J. W., "Active Flow Control for Interaction Noise Reduction of Contra-Rotating Open Rotors," *AIAA Journal*, Vol. 54, No. 4, 2016, pp. 1413–1423. https://doi.org/10.2514/1.J053756.

[12] Zachariadis, A., Hall, C., and Parry, A. B., "Contrarotating Open Rotor Operation for Improved Aerodynamics and Noise at Takeoff," *Journal of Turbomachinery*, Vol. 135, 2013. https://doi.org/10.1115/1.4006778.

[13] Delattre, G., and Falissard, F., "Influence of Torque Ratio on Counter-Rotating Open-Rotor Interaction Noise," *AIAA Journal*, Vol. 53, No. 9, 2015, pp. 2726–2738. https://doi.org/10.2514/1.J053797.

[14] International Civil Aviation Organization, "CHAPTER 10. Propeller-driven aeroplanes not exceeding 8 618 kg," *ICAO Annex 16: Environmental Protection Volume 1 - Aircraft Noise*, 2011.

[15] Filippone, A., and Mohamed-Kassim, Z., "Multi-disciplinary simulation of propeller-turboprop aircraft flight," *Aeronautical Journal*, Vol. 116, No. 1184, 2012, pp. 985–1014. https://doi.org/10.1017/S0001924000007454.

[16] Filippone, A., "Aircraft Noise: Noise Sources," *Advanced Aircraft Flight Performance*, Cambridge University Press, 2012, pp. 470–532. https://doi.org/10.1017/CBO9781139161893.

[17] Jeracki, R. J., Mikkelson, D. C., and Blaha, B. J., "Wind Tunnel Performance of Four Energy Efficient Propellers Designed for Mach 0.8 Cruise," *NASA TM-79124*, 1979. https://doi.org/10.4271/790573.

[18] Smith, D. A., Filippone, A., and Bojdo, N., "Low Order Multidisciplinary Optimisation of Counter-Rotating Open Rotors," *European Rotorcraft Forum*, Delft, 2018.

[19] Barakos, G., Steijl, R., Badcock, K., and Brocklehurst, A., "Development of CFD Capability for Full Helicopter Engineering Analysis," *31st European Rotorcraft Forum*, 2005.

[20] Steijl, R., Barakos, G., and Badcock, K., "A Framework for CFD Analysis of Helicopter Rotors in Hover and Forward Flight." *International Journal for Numerical Methods in Fluids*, Vol. 51, No. 8, 2006, pp. 819–847. https://doi.org/10.1002/fld.1086.

[21] Jarkowski, M., Woodgate, M. A., Barakos, G. N., and Rokicki, J., "Towards Consistent Overset Mesh Methods for Rotorcraft CFD," *International Journal for Numerical Methods in Fluids*, Vol. 74, 2014, pp. 543–576. https://doi.org/10.1002/fld.3861.

[22] Hirt, C., Amsden, A., and Cook, J., "An Arbitrary Lagrangian–Eulerian Computing Method for All Flow Speeds," *Journal of Computational Physics*, Vol. 135, No. 2, 1997, pp. 203–216. https://doi.org/10.1006/jcph.1997.5702.

[23] Menter, F. R., "Two-equation eddy-viscosity turbulence models for engineering applications," *AIAA Journal*, Vol. 32, No. 8, 1994, pp. 1598–1605. https://doi.org/10.2514/3.12149.

[24] Osher, S., and Chakravarthy, S., "Upwind schemes and boundary conditions with applications to Euler equations in general geometries," *Journal of Computational Physics*, Vol. 50, No. 3, 1983, pp. 447–481. https://doi.org/10.1016/0021-9991(83)90106-7.

[25] van Leer, B., "Towards the ultimate conservative difference scheme. V. A second-order sequel to Godunov's method," *Journal of Computational Physics*, Vol. 32, No. 1, 1979, pp. 101–136. https://doi.org/10.1016/0021-9991(79)90145-1.

[26] van Albada, G. D., van Leer, B., and Roberts Jr., W. W., "A Comparative Study of Computational Methods in Cosmic Gas Dynamics," *Astronomy and Astrophysics*, Vol. 108, No. 1, 1982, pp. 76–84. https://doi.org/10.1007/978-3-642-60543-7_6.

[27] Axelsson, O., *Iterative Solution Methods*, Cambridge University Press, 1994. https://doi.org/10.1016/j.apnum.2004.06.003.

[28] Chirico, G., Barakos, G. N., and Bown, N., "Computational Aeroacoustic Analysis of Propeller Installation Effects," *43rd European Rotorcraft Forum*, 2017.

[29] Jimenez-Garcia, A., Barakos, G. N., and Gates, S., "Tiltrotor CFD Part I - Validation," *Aeronautical Journal*, Vol. 121, No. 1239, 2017, pp. 577–610. https://doi.org/10.1017/aer.2017.17.

[30] Dunham, D. M., Gentry, C. L., and Coe, P. L., "Low-Speed Wind-Tunnel Tests of Single- and Counter-Rotation Propellers," *NASA TM-87656*, 1986.

[31] Farassat, F., "Linear Acoustic Formulas for Calculation of Rotating Blade Noise," *AIAA Journal*, Vol. 19, No. 9, 1981, pp. 1122–1130. https://doi.org/10.2514/3.60051.

[32] Ffowcs Williams, J. E., and Hawkings, D. L., "Sound Generation by Turbulence and Surfaces in Arbitrary Motion," *Philosophical Transactions of the Royal Society A: Mathematical, Physical and Engineering Sciences*, Vol. 264, No. 1151, 1969, pp. 321–342. https://doi.org/10.1098/rsta.1969.0031.

[33] Parry, A. B., Kingan, M., and Tester, B. J., "Relative importance of open rotor tone and broadband noise sources," *17th AIAA/CEAS Aeroacoustics Conference 2011 (32nd AIAA Aeroacoustics Conference)*, 2011. https://doi.org/10.2514/6.2011-2763.

[34] Kingan, M. J., "Open Rotor Broadband Interaction Noise," *Journal of Sound and Vibration*, Vol. 332, No. 17, 2013, pp. 3956–3970. https://doi.org/10.1016/j.jsv.2013.03.014.

[35] Block, P. J. W., Klatte, R. J., and Druez, P. M., "Counter-Rotating Propeller Noise Directivity and Trends," *AIAA 10th Aeroacoustics Conference*, Seattle, Washington, 1986. https://doi.org/10.2514/6.1986-1927.

[36] Filippone, A., "6. Propeller Performance," *Advanced Aircraft Flight Performance*, 2012, pp. 152–178.

[37] Kingan, M. J., Ekoule, C. M., Parry, A. B., and Britchford, K. M., "Analysis of Advanced Open Rotor Noise Measurements," *20th AIAA/CEAS Aeroacoustics Conference*, 2014. https://doi.org/10.2514/6.2014-2745.

[38] Kingan, M. J., and Self, R. H., "Counter-Rotation Propeller Tip Vortex Interaction Noise," *15th AIAA/CEAS Aeroacoustics Conference (30th AIAA Aeroacoustics Conference)*, 2009. https://doi.org/10.2514/6.2009-3135.

[39] Haller, G., "An objective definition of a vortex," *Journal of Fluid Mechanics*, Vol. 525, 2005. https://doi.org/10.1017/S0022112004002526.